

RESEARCH ARTICLE

10.1002/2017JA024700

Key Points:

- The interplanetary propagation of 15 CMEs is studied based on a cross-correlation analysis of Forbush decreases at 1 AU and Mars
- The speed evolutions of the ICMEs are derived from observations, indicating that most of them are slightly decelerated even beyond 1 AU
- Model-predicted ICME arrival times at Mars could be improved by using ICME parameters measured at 1 AU

Correspondence to:

J. Guo,
guo@physik.uni-kiel.de

Citation:

Freiherr von Forstner, J. L., Guo, J., Wimmer-Schweingruber, R. F., Hassler, D. M., Temmer, M., Dumbović, M., ... Zeitlin, C. J. (2018). Using Forbush decreases to derive the transit time of ICMEs propagating from 1 AU to Mars. *Journal of Geophysical Research: Space Physics*, 123, 39–56. <https://doi.org/10.1002/2017JA024700>

Received 23 AUG 2017

Accepted 18 DEC 2017

Accepted article online 3 JAN 2018

Published online 18 JAN 2018

Using Forbush Decreases to Derive the Transit Time of ICMEs Propagating from 1 AU to Mars

Johan L. Freiherr von Forstner¹ , Jingnan Guo¹ , Robert F. Wimmer-Schweingruber¹, Donald M. Hassler^{2,3}, Manuela Temmer⁴ , Mateja Dumbović⁴, Lan K. Jian^{5,6} , Jan K. Appel¹ , Jaša Čalogović⁷, Bent Ehresmann², Bernd Heber¹ , Henning Lohf¹, Arik Posner⁸, Christian T. Steigies¹, Bojan Vršnak⁷, and Cary J. Zeitlin⁹

¹Institute of Experimental and Applied Physics, University of Kiel, Kiel, Germany, ²Southwest Research Institute, Boulder, CO, USA, ³Institut d'Astrophysique Spatiale, University Paris Sud, Orsay, France, ⁴Institute of Physics, University of Graz, Graz, Austria, ⁵Department of Astronomy, University of Maryland, College Park, MD, USA, ⁶Heliophysics Science Division, NASA Goddard Space Flight Center, Greenbelt, MD, USA, ⁷Hvar Observatory, Faculty of Geodesy, University of Zagreb, Zagreb, Croatia, ⁸NASA Headquarters, Washington, DC, USA, ⁹Leidos, Houston, TX, USA

Abstract The propagation of 15 interplanetary coronal mass ejections (ICMEs) from Earth's orbit (1 AU) to Mars (~1.5 AU) has been studied with their propagation speed estimated from both measurements and simulations. The enhancement of magnetic fields related to ICMEs and their shock fronts causes the so-called Forbush decrease, which can be detected as a reduction of galactic cosmic rays measured on ground. We have used galactic cosmic ray (GCR) data from in situ measurements at Earth, from both STEREO A and STEREO B as well as GCR measurements by the Radiation Assessment Detector (RAD) instrument on board Mars Science Laboratory on the surface of Mars. A set of ICME events has been selected during the periods when Earth (or STEREO A or STEREO B) and Mars locations were nearly aligned on the same side of the Sun in the ecliptic plane (so-called opposition phase). Such lineups allow us to estimate the ICMEs' transit times between 1 and 1.5 AU by estimating the delay time of the corresponding Forbush decreases measured at each location. We investigate the evolution of their propagation speeds before and after passing Earth's orbit and find that the deceleration of ICMEs due to their interaction with the ambient solar wind may continue beyond 1 AU. We also find a substantial variance of the speed evolution among different events revealing the dynamic and diverse nature of eruptive solar events. Furthermore, the results are compared to simulation data obtained from two CME propagation models, namely the Drag-Based Model and ENLIL plus cone model.

Plain Language Summary Eruptions from the Sun often containing a shock front followed by a magnetic ejecta may cause a depression in the omnipresent cosmic rays that can now be observed at Mars thanks to the radiation assessment detector (RAD) on board the Mars Science Laboratory. When both Earth (or other spacecraft like STEREOs that are located at Earth orbit) and Mars are closely aligned on the same side of the Sun, we have a great opportunity to observe such eruptions passing by and affecting both planets. Based on measurements from both Earth orbit and Mars, we have studied 15 solar events and their properties such as the speed and its evolution from the Sun to Mars. We found that most of these eruptions slow down considerably during their propagation from the Sun to Earth orbit and even beyond all the way to Mars.

1. Introduction

It is currently well accepted that coronal mass ejections (CMEs), magnetized plasma clouds expelled from the Sun, may have severe impact on Earth, robotic missions on other planets, and spacecraft electronics. A better understanding of the interplanetary propagation of CMEs is very important to gain a deeper understanding of the heliosphere and the Sun itself, and to improve space weather forecasting.

ICMEs are regularly observed using both remote sensing images (coronagraph and heliospheric imaging instruments) and in situ measurements of plasma and magnetic field quantities (e.g., Richardson & Cane, 1995; Wimmer-Schweingruber et al., 2006). Another common in situ method to detect ICMEs employs the

observation of Forbush decreases (FD, first observed by Forbush, 1937; Hess & Demmelmair, 1937 and also studied by, e.g. Burlaga et al., 1985; Cane, 2000; Kumar & Badruddin, 2014; Lockwood, 1971; Zhao & Zhang, 2016) in measurements of galactic cosmic rays (GCRs) caused by the magnetic field structure embedded in the ICME passing by.

ICMEs do not necessarily consist only of the magnetized ejecta (which, depending on its geometry, can also be called “magnetic cloud” or “flux rope”), but in many cases also drive an interplanetary shock in front of them, separated by a turbulent sheath region. Forbush decreases can occur during the passage of the sheath region (after the shock arrival) as well as the ejecta, which is described to be the cause of a two-step structure, for example, by Cane (2000). However, recent studies such as Jordan et al. (2011) and Masías-Meza et al. (2016) have found that even though the ejecta is effective at decreasing the GCR intensity, an ICME with a shock does not necessarily produce a clear two-step structure in the FD and that the shock arrival is much more likely to produce an abrupt drop in the GCR intensity than the ejecta. When multiple CMEs are ejected from the Sun in a short period of time, they can interact with each other during their propagation and form complex structures, which also affects the corresponding Forbush decrease (e.g., Maričić et al., 2014).

The interplanetary propagation of ICMEs is strongly influenced by the ambient solar wind. This leads to either a deceleration or acceleration depending on the relative speed of the ICME to the ambient solar wind speed (e.g., Gopalswamy et al., 2001; Vršnak et al., 2004; Vršnak & Žic, 2007). As most CMEs launched from the Sun are faster than the ambient solar wind, this more often results in deceleration rather than acceleration. With a large amount of imaging and in situ instruments available on spacecraft especially near Earth’s orbit, extensive studies of the evolution of CMEs during their eruption at the Sun and their propagation up to 1 AU have been carried out. Heliospheric imaging instruments, for example, on board the two *Solar Terrestrial Relations Observatory* (STEREO) spacecraft allow a continuous tracking of ICMEs up to 1 AU (e.g., Lugaz et al., 2012; Möstl et al., 2014; Wood et al., 2017). Additionally, spacecraft such as *Ulysses* (e.g., Jian et al., 2008; Wang et al., 2005) and *Voyager* (e.g., Liu et al., 2014) have provided ICME observations at locations in the outer solar system. Based on the results from Wang et al. (2005) and their own studies of ICMEs seen at Mercury and Earth, Winslow et al. (2015) stated that the deceleration of most ICMEs should cease at approximately 1 AU.

With the *Curiosity* rover of NASA’s *Mars Science Laboratory* (MSL) mission (Grotzinger et al., 2012), another device capable of registering Forbush decreases is available on the surface of Mars (at approximately 1.5 AU) since its landing on 6 August 2012. Its *Radiation Assessment Detector* (RAD) instrument (Hassler et al., 2012) has been continuously measuring GCR particles on the surface of Mars since then. MSL/RAD was already used for observations of ICMEs through Forbush decreases, for example, by Witasse et al. (2017).

In situ observations of ICMEs at Mars are also possible using instruments on the *Mars Atmosphere and Volatile Evolution* (MAVEN) spacecraft that is in orbit around Mars. But it only arrived at Mars in September 2014, so a time period of 2 years after MSL’s arrival cannot be studied using MAVEN data. For this reason, we have not yet incorporated MAVEN data in this study, but we plan to do so in the future as the number of ICMEs observed by MAVEN increases. A first study involving a comparison of ICME measurements at MAVEN and MSL/RAD can be found in Guo, Lillis, et al. (2017).

At times where Mars and either Earth or the STEREO A or STEREO B spacecraft have a low separation in their heliospheric longitudes, that is, they nearly form a straight line with the Sun, we have a better chance of observing the same ICMEs at both 1 AU and Mars using in situ data. These times are the oppositions of Mars observed from Earth and the STEREO spacecraft, respectively. We define an *opposition phase* to be the period where the absolute value of the longitudinal separation $\Delta\varphi$ between Mars and Earth (or STEREO) is smaller than a fixed value $\Delta\varphi_{\max}$, which for this study is set to 30° , keeping the probability that ICMEs are observed at both locations reasonably high, but at the same time not restricting the number of ICME candidates too much. The latitudinal separations between Earth, the STEREO spacecraft, and Mars are generally only a few degrees at most and therefore not taken into account. Yashiro et al. (2004) found that the average angular width of CMEs is between 47° and 61° , which supports that choosing $\Delta\varphi_{\max} = 30^\circ$ is reasonable. Figure 1 illustrates the opposition phases and the definition of $\Delta\varphi_{\max}$.

These multispacecraft observations of ICMEs during the opposition phases allow us to determine ICMEs’ travel times between the radial distances of 1 AU and ~ 1.5 AU from the Sun. They can be used to compare the resulting transit speed with measurements at 1 AU to determine the amount of deceleration or acceleration.

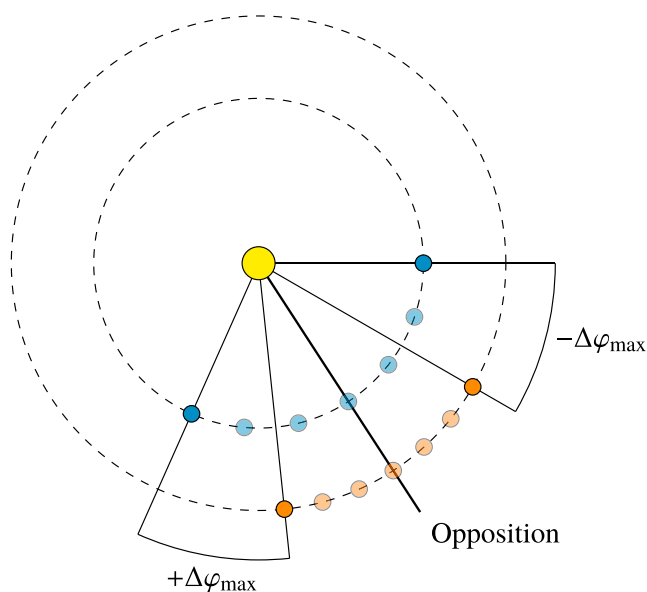


Figure 1. The opposition phases for this study are defined by the longitudinal separation of Earth (or STEREO) and Mars being between $-\Delta\varphi_{\max}$ and $+\Delta\varphi_{\max}$. The bold diagonal line marks the opposition itself.

To be able to derive the propagation time of an ICME between the two observation locations, we assume that the same part of the ICME is observed at both places, or alternatively that the ICME's shape has a sufficient amount of radial symmetry between the two longitudes where it is observed. The probability that this assumption holds true is obviously higher for smaller longitudinal separations of the two observers, which is another reason why we chose a small angle for $\Delta\varphi_{\max}$. A sophisticated study of the ICMEs' shapes could only in theory be done with a significantly higher number of observation locations or using 3-D reconstruction techniques based on stereoscopic imaging techniques, where the former drastically reduces the amount of ICME candidates and the latter can currently only be done up to approximately 1 AU, for example, with the heliospheric imagers at both STEREO spacecraft (e.g., Liu et al., 2010).

2. Methods and Data

2.1. Data

Table 1 shows the opposition periods between CURIOSITY's landing in August 2012 and the end of 2016, as defined in Figure 1. Oppositions of Earth and Mars are included as well as those with the STEREO spacecraft.

We used the ICME list by Richardson and Cane (2010) (<http://www.srl.caltech.edu/ACE/ASC/DATA/level3/icmetable2.htm>) as a basis for finding the ICME-caused Forbush decreases at Earth and a similar list by Jian et al. (2013) for ICMEs at STEREO A and STEREO B.

Communication with the STEREO B spacecraft was lost on 1 October 2014 and a recovery attempt in summer 2016 was not successful. Therefore, data from its 2015 opposition with Mars are not available. Additionally, because of the solar conjunction in 2015, the Plasma and Suprathermal Ion Composition (PLASTIC) instrument on board STEREO A was turned off and there is no plasma data for the second STEREO A and Mars opposition phase. For these reasons, we excluded the two 2015 opposition phases, leaving us with the four opposition periods to investigate in this study.

For the two oppositions of Earth and Mars, we retrieved count rate data from the Neutron Monitor Database (<http://nmdb.eu>). We chose the South Pole neutron monitor, which has a low cutoff rigidity (with an effective vertical cutoff rigidity of 0.1 GV) due to its geographic location. This was then used together with the RAD dose rate data to apply the cross-correlation method, which will be described in section 2.3.

For the STEREO oppositions, we replaced the neutron monitor count rates with measurements from the High Energy Telescope (HET) instruments available on both STEREO spacecraft (von Rosenvinge et al., 2008), which measure the flux of high-energy charged particles. While in situ observations of ICMEs at the STEREO spacecraft are also possible using magnetometer and plasma data (as has been used to identify ICMEs in the lists employed in our study), Forbush decreases in the HET data allow for a more direct comparison to the RAD data at Mars.

The publicly available HET data include measurements of protons with kinetic energies between 13.6 and 100 MeV and electrons between 0.7 and 4.0 MeV, with each of these ranges subdivided into multiple

Table 1
Opposition Periods Considered for This Study

Opposition type	Date		
	Start	Opposition	End
STEREO B and Mars	2012-8-22	2012-11-28	2013-2-5
STEREO A and Mars	2013-5-21	2013-7-19	2013-9-12
Earth and Mars	2014-2-13	2014-4-8	2014-6-10
Earth and Mars	2016-3-20	2016-5-22	2016-8-5

Note. The start and end dates of the $\pm 30^\circ$ periods and the actual date of the opposition are given. Dates are formatted as year/month/day.

energy bins. We chose the 23.8 and 100 MeV proton range, which appeared to show the Forbush decreases reasonably well for this study. In some cases (event numbers 1, 2, 4, 5, 7, and 9), we chose to only use the highest-energy channel (60 and 100 MeV) instead because there were solar energetic particles (SEP) coinciding with the ICME arrival at STEREO, resulting in a much higher particle flux instead of FDs in the lower HET channels.

2.2. RAD Data and Compensating for the Diurnal Variations

RAD/MSL is an energetic particle detector, and it has been carrying out radiation measurements on the surface of Mars since the landing of MSL in August 2012 (Ehresmann et al., 2014; Guo et al., 2015; Guo, Slaba, et al., 2017; Hassler et al., 2014; Köhler et al., 2014; Rafkin et al., 2014; Wimmer-Schweingruber et al., 2015). On the surface of Mars, RAD measures a mix of primary GCRs or SEPs and secondary particles generated in the atmosphere including both charged and neutral particles. Due to the shielding of the atmosphere, such particles are mostly equivalent to primary GCR/SEP with energies larger than ~ 100 MeV/nuc. The radiation dose rates contributed by surface particles are measured in two detectors—a silicon detector and a plastic scintillator—and the latter has better statistics due to a larger geometric factor and is a very good proxy for studying GCR fluence and its temporal variations.

RAD's GCR dose rate measurements on the surface of Mars show a considerable amount of periodic variation (about $\pm 5\%$) with a frequency of 1 sol and its harmonics, which is caused by the variation of temperature and therefore atmospheric pressure during the course of the Martian day. This effect was analyzed by Rafkin et al. (2014), and its intensity varies for different fluxes of primary and secondary GCR particles.

Guo, Slaba, et al. (2017) found that the magnitude of this diurnal effect is not constant but rather influenced by the solar modulation of the primary GCRs; direct subtracting of the pressure effect during an FD event is therefore not feasible. To reliably detect Forbush decreases in this data, we process the data using a notch filter (Parks & Burrus, 1987) that significantly reduces the diurnal variations in the data but keeps other influences—such as Forbush decreases—intact. A more detailed description of the implementation of this method is shown in Guo, Lillis, et al. (2017).

2.3. Cross-Correlation Analysis

We assume that the traveltime of the ICMEs between 1 AU and Mars corresponds to the delay time between the onset of Forbush decreases detected at these two locations. To determine this delay, we use a method based on the cross-correlation function (CCF), assuming that Forbush decreases at 1 AU and Mars from the same ICME should have similar characteristics, such as being a one- or two-step decrease. An advantage of this method is that it allows to determine the traveltime without needing to define exact onset times at both Earth and Mars, which can be difficult when the Forbush decrease is weak and/or rather complex.

For the analysis, a ± 1 sol window (a sol is a solar day on Mars, $1 \text{ sol} \approx 24 \text{ h } 40 \text{ m}$) around the given ICME onset time at 1 AU $t_{1 \text{ AU}}$ is selected from the GCR data at 1 AU, which includes a Forbush decrease at this time. The rather small window makes sure that we only compare the actual decrease, so that a difference in the following recovery period should not affect the results. The normalized cross-correlation function of the 1 AU data with the filtered RAD dose rate data (see details in section 2.2) is then calculated in this window. It is a measure for the correlation between the two data sets when one is shifted in time by a lag τ . For discrete measurements $f[m]$ and $g[m]$, the normalized cross-correlation function is defined as

$$(f \star g)[n] \doteq \frac{1}{m_{\max} - m_{\min}} \sum_{m=m_{\min}}^{m_{\max}} f'[m] g'[m+n], \quad (1)$$

where the lag τ is represented by a number of data points n , the range $[m_{\min}, m_{\max}]$ is the aforementioned ± 1 sol window, and the normalized functions f' and g' are defined as

$$\begin{aligned} f'[m] &\doteq \frac{f[m] - \bar{f}}{\sigma_f}, \\ g'[m] &\doteq \frac{g[m] - \bar{g}}{\sigma_g}. \end{aligned} \quad (2)$$

where σ_f and σ_g are standard deviations of $f[m]$ and $g[m]$ in the range $[m_{\min}, m_{\max}]$, respectively.

The value of τ where $(f \star g)$ assumes its maximum in a reasonable range $\tau \in [0, \Delta t_{\max}]$ is considered to be the ICME's traveltime T between 1 AU and Mars. We fit the cross-correlation function's peak with a Gaussian distribution to estimate the error of T .

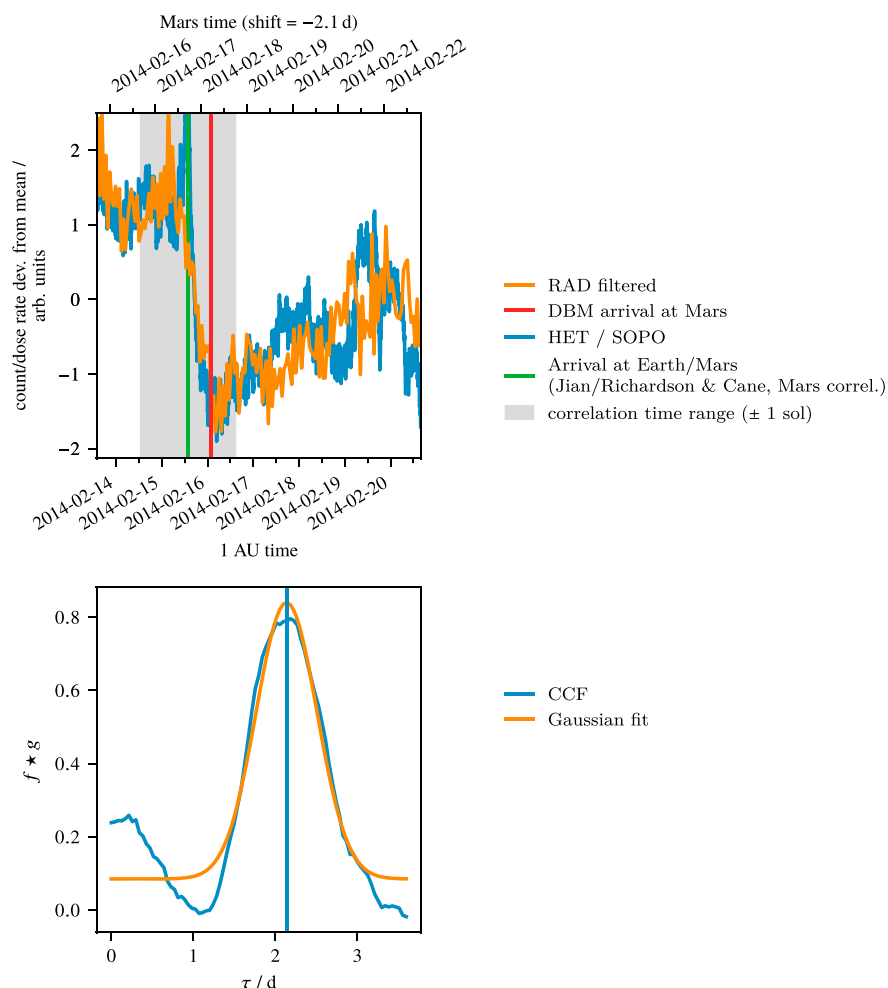


Figure 2. Example of an application of the cross-correlation method. (top) The count rate data from the South Pole neutron monitor with the ICME disturbance time from the Richardson and Cane ICME list marked by the green bar. In the same panel, the RAD dose rate data (filtered using the method described in section 2.2 and shifted back in time by the best fitted CCF lag time) are shown, together with the onset time calculated using the Drag-Based Model (DBM) (red bar). (bottom) The cross-correlation function (CCF) of the two data sets plotted over the time lag τ , fitted with a Gaussian function to obtain the estimated traveltime T and its uncertainty. The window used for calculating the CCF is displayed in Figure 2 (top) with a light gray color. In this example, the resulting ICME traveltime is 2.14 ± 0.37 days, which is slightly shorter than the 2.6 days calculated using the DBM (explained later in section 3.3).

Figure 2 shows an example of an application of the cross-correlation method applied to the ICME that arrived at Earth on 15 February 2014. The implication of these results will be discussed in section 3.1.

The GCR data in Figure 2 is scaled so that the correlation between the two data sets is more clearly shown. Specifically, we subtract the mean value in the shown time range from the measurements and then divide the results by their standard deviations. For some events at the STEREO spacecraft, we adjusted the scaling of the HET flux rate data manually as the calculation of the mean and standard deviation was affected by strong increases in the data related to SEP events shortly before or after the ICME arrival. This was done by calculating the mean and standard deviation in a smaller ± 16 h period around $t_{1 \text{ AU}}$ instead of the whole range of the plot. Additionally, in one case (event 1) we needed to decrease the size of the window in which the correlation is calculated to ± 0.75 sol instead of ± 1 sol to make sure that the SEP event does not influence the result of the cross-correlation analysis.

Note that we are not comparing the magnitude of the Forbush decreases at 1 AU and Mars, which would be an interesting study in the future. However, it needs to be considered that both the neutron monitor

measurements and RAD dose rate are influenced by the atmosphere and/or magnetosphere of two different planets, which makes the comparison more complicated than simply assessing the relative drop ratios in the two data sets.

3. Results and Discussion

3.1. Results

In total, 43 ICMEs were observed during the four opposition periods, according to the Richardson/Cane (Richardson & Cane, 2010) and Jian (Jian et al., 2013) lists. However, not all of them caused visible Forbush decreases in our data sets at 1 AU and/or Mars—probably because (a) FDs can be very weak in comparison to the background oscillations, for example, due to low ICME speeds and/or magnetic field strengths; (b) the ICME missed one of the observation points, for example, due to (1) the angular width of the ICME is not covering the longitudinal separation of 1 AU and Mars observers (up to $\pm 30^\circ$) and/or (2) a significant deviation of the propagation direction; (c) a gap occurring in the data at one of the observation locations; or (d) a strong solar energetic particle (SEP) event seen at STEREO does not allow us to see the FD even when selecting only the highest-energy channels.

Additionally, a considerable amount of ICMEs were ejected from the Sun in quick succession and possibly interacted or merged with each other during their propagation, which makes the cross-correlation analysis very difficult. One example for this is a series of five events in early February 2014 at Earth, where only the first event could be analyzed sufficiently well using the cross-correlation method as its distance to the others was larger and it had the strongest FD.

We therefore only kept the events in the study where the onset time from the list corresponded to a clear FD at 1 AU and where a convincing correspondence to a FD at Mars could be found using the cross-correlation analysis. For the 15 remaining events, we are most confident that the cross-correlation method picked up the Forbush decreases corresponding to the same ICME in the data sets at both locations.

In total, 14 events had no or only weak Forbush decreases at at least one of the observation locations causing a high uncertainty in the cross-correlation method results; 10 events were dropped due to a merging of multiple ICMEs, 3 FDs at STEREO could not be seen due to a coinciding SEP event; and one event could not be analyzed due to a gap in the RAD data. A comparison of the speeds v_{\max} listed in the Richardson and Cane/Jian lists of the full set of 43 events to our selection of 15 events shows that both nearly have the same average value of 476 km s^{-1} and 475 km s^{-1} , respectively, so it seems that we did not select a set of particularly fast ICMEs.

The Richardson/Cane and Jian lists include arrival times for multiple ICME features: The disturbance arrival time (which refers to the arrival of a shock), the ICME plasma arrival time, and the ICME end time. For the ICMEs where the disturbance arrival time was listed, we used it as the basis for the cross-correlation method because as explained in section 1, the shock is most likely to cause the FD. For the remaining events, we used the ICME plasma arrival time.

In fact, the choice of the onset time used at Earth hardly affects our study of the propagation time as it is only used to determine the position of the ± 1 sol window (which is sufficiently large in comparison to the onset time precision) in which the cross-correlation function is calculated. Nevertheless, in a few cases (events 11–13) the onset times were manually corrected “by eye” by amounts of up to a few hours to better reflect the beginning of the Forbush decrease in the in situ data at Earth, which is not necessarily equal to the start of the disturbance or ICME start given in the lists.

Table 2 shows the basic data and the results of the cross-correlation method for all the ICMEs in this study. Figures A1–A5 in Appendix A include the corresponding plots of the in situ data and CCF.

As explained in section 2.3, due to the uncertainties in the data, the CCF was fitted with a Gaussian distribution to both enhance the detection of the maximum and obtain an estimation of the error. This method works reasonably well most of the time, but in some cases (e.g. events 9 and 14), the CCF shows a relatively wide peak, overlaid by one or multiple narrow peaks. Especially in these cases, the error might have been overestimated by the fit, which generally follows the wide peak.

For each ICME, the ratio $\bar{v}/v_{1 \text{ AU}}$ was calculated and shown Table 2, where $v_{1 \text{ AU}}$ is the measured maximum speed of the ICME at 1 AU, obtained from the Richardson/Cane and Jian lists (v_{\max} column—maximum solar wind speed during the passing of the ICME and shock/sheath), which presumably corresponds to the propagation speed of the shock (if present) or the ejecta; and \bar{v} is the average speed of the ICME between 1 AU and

Table 2
Table of All the ICMEs Examined in This Study

ICME	Obs S/C	Observations					Cross-correlation method results			
		t_1 AU (UTC)	v_1 AU /km s ⁻¹	Δr /AU	v_{launch} /km s ⁻¹	v_{sw} /km s ⁻¹	T_{correl} /days	$t_{\text{Mars}} = t_1 \text{ AU} + T_{\text{correl}}$ (UTC)	\bar{v} /km s ⁻¹	$\frac{\bar{v}}{v_1 \text{ AU}}$
1	STB	2012-9-25 16:26	740.0	0.407	1056	389±12	1.24±0.23	2012-9-26 22:13	567±103	0.77±0.14
2	STB	2012-10-17 06:57	365.0	0.369	960	295±5	2.05±0.33	2012-10-19 08:16	311±51	0.85±0.14
3	STB	2012-10-25 19:10	435.0	0.357	380	297±5	2.31±0.66	2012-10-28 02:39	267±76	0.61±0.17
4	STB	2012-11-11 13:36	512.0	0.334	710	333±22	1.33±0.46	2012-11-12 21:27	436±150	0.85±0.29
5	STB	2012-11-19 09:50	505.0	0.326	643	344±6	1.50±0.54	2012-11-20 21:47	377±137	0.75±0.27
6	STB	2012-11-28 03:36	347.0	0.318	440	331±7	1.46±0.27	2012-11-29 14:32	378±71	1.09±0.20
7	STA	2013-5-29 12:20	480.0	0.516	879	398±20	2.53±0.37	2013-6-1 00:57	354±51	0.74±0.11
8	STA	2013-6-27 16:17	397.0	0.551	732	343±20	2.53±0.48	2013-6-30 04:54	377±72	0.95±0.18
9	STA	2013-7-25 06:12	545.0	0.584	1000	325±23	2.57±0.56	2013-7-27 19:50	393±85	0.72±0.16
10	STA	2013-8-10 15:00	453.0	0.603	375	367±15	2.57±0.24	2013-8-13 04:38	407±38	0.90±0.08
11	EARTH	2014-2-15 13:45	450	0.669	620	342±10	2.14±0.37	2014-2-17 17:07	541±93	1.20±0.21
12	EARTH	2014-4-5 19:00	500	0.624	450	419±22	1.84±0.72	2014-4-7 15:10	587±230	1.17±0.46
13	EARTH	2014-4-18 19:00	500	0.609	396	366±30	2.40±0.71	2014-4-21 04:32	440±131	0.88±0.26
14	EARTH	2016-3-20 07:00	430	0.602		432±19	3.00±0.61	2016-3-23 06:55	348±71	0.81±0.16
15	EARTH	2016-8-2 14:00	460	0.418	350	350±18	2.40±0.53	2016-8-4 23:32	302±66	0.66±0.14
Average			475	0.486	642	355±4	2.12±0.13		406±27	0.86±0.06

Note. The second column shows the spacecraft or planet at 1 AU where the ICME was observed (STEREO A, STEREO B, or Earth), and the third column contains the ICME arrival time t_1 AU at this location according to the Richardson/Cane or Jian list (disturbance start time if available, otherwise ICME start time). The fourth column states the speed v_1 AU, also taken from the Richardson/Cane and Jian lists (v_{max}). Δr is the radial distance between Earth and Mars or the STEREO spacecraft and Mars, respectively, at the time t_1 AU. The next two columns include the CME launch speed v_{launch} used for simulation purposes and the average ambient solar wind speed v_{sw} in 3 days before the ICME arrival at 1 AU. T_{correl} is the estimated traveltime obtained from the cross-correlation method. The arrival time at Mars t_{Mars} was calculated under the assumption that t_1 AU is correct, and \bar{v} is the average ICME speed between Earth orbit and Mars calculated from T_{correl} and Δr . The final column shows the ratio \bar{v}/v_1 AU. The last row shows the average values (if applicable) for all events together.

Mars calculated from the traveltime obtained from the cross-correlation method and the radial distance Δr between Earth (or the STEREO spacecraft) and Mars:

$$\bar{v} = \frac{\Delta r}{T_{\text{correl}}}. \quad (3)$$

Additionally, if we assume that the acceleration a of the ICME between 1 AU and Mars is constant, we can calculate it from the traveltime T_{correl} and the measured speed at 1 AU using the following considerations: With $v(t) = v_1 \text{ AU} + at$, the mean speed \bar{v} (as given in equation (3) can also be expressed as

$$\bar{v} = \frac{\int_0^{T_{\text{correl}}} v(t) dt}{T_{\text{correl}}} = v_1 \text{ AU} + \frac{1}{2} a T_{\text{correl}}.$$

Equating this expression with the one from equation (3) and solving for a give

$$a_{1 \text{ AU}, \text{ Mars}} = 2 \left(\frac{\Delta r}{T_{\text{correl}}^2} - \frac{v_1 \text{ AU}}{T_{\text{correl}}} \right). \quad (4)$$

This value was also calculated for all events and included in Table 2. Similarly, the mean acceleration between a radial distance of $21.5 R_{\odot}$ from the Sun and the arrival at 1 AU, $a_{\text{Sun}, 1 \text{ AU}}$, was calculated using the speed at $21.5 R_{\odot}$ obtained from the Database of Notifications, Knowledge, Information (DONKI) database (section 3.3) and the traveltime between those locations. In the case of ICME 2, the launch speed of 480 km s^{-1} from the DONKI database was changed to the more reasonable value of 960 km s^{-1} reported in the SOHO/LASCO CME catalog for the calculation of the acceleration. The DONKI value of 480 km s^{-1} led to a negative, unphysical result for the drag parameter Γ calculated in section 3.4. For the other events, the difference between the DONKI and SOHO/LASCO catalogs was much less significant.

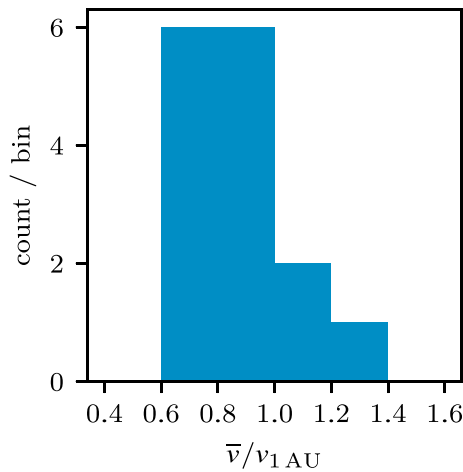


Figure 3. Histogram of ICME speed changes between 1 AU and Mars. Plotted is the ratio of the calculated mean speed between 1 AU and Mars over the measured speed at 1 AU.

3.2. Statistical Analysis

In Figure 3, we show a histogram of the ratio $\bar{v}/v_{1 \text{ AU}}$ for the 15 ICMEs. On average, we get a value of

$$\left\langle \frac{\bar{v}}{v_{1 \text{ AU}}} \right\rangle = 0.86 \pm 0.06,$$

which indicates that the average ICME in our sample decelerates slightly during its propagation between 1 and 1.5 AU.

Considering the calculated standard deviations σ of the $\bar{v}/v_{1 \text{ AU}}$ values (included in Table 2) and using a 1σ confidence interval, we can say that eight ICMEs (53% of our sample of ICMEs) decelerated ($\bar{v}/v_{1 \text{ AU}} + \sigma < 1$) and no ICME accelerated ($\bar{v}/v_{1 \text{ AU}} - \sigma > 1$) while the seven remaining events showed neither a clear deceleration nor acceleration. We calculated the mean and standard deviation of $v_{1 \text{ AU}}$ of our 15 events to be 466.9 km s^{-1} and 84.5 km s^{-1} , respectively, while the mean and standard deviation of $v_{1 \text{ AU}}$ of all ICMEs in the Richardson and Cane list from 2012 until 2016 (123 events) are 489.2 km s^{-1} and 114.2 km s^{-1} . Despite of the small sample of our events, the $v_{1 \text{ AU}}$ measurements seem to suggest that they are good

in representing the average ICME speeds at 1 AU. However, we still note that our derived probabilities of the changing of ICME speeds should be applied with caution because (a) our accuracy is not high enough to find out the exact speed change of the remaining seven events, and (b) the geometry of the ICME may affect our results, which will be discussed in more detail later (see also Figures 5 and 6).

As the deceleration of ICMEs is believed to be related to the ambient solar wind speed, we also compared the $\bar{v}/v_{1 \text{ AU}}$ values to the solar wind speed v_{sw} in Figure 4, using data from the *Solar Wind Electron, Proton, and Alpha Monitor* (SWEPAM) instrument (McComas et al., 1998) on the *Advanced Composition Explorer* (ACE) spacecraft (Stone et al., 1998) located at the L1 point near Earth and the *Plasma and Suprathermal Ion Composition* (PLASTIC) (Galvin et al., 2008) instruments on the two STEREO spacecraft. The value we used for v_{sw} is the average value of the solar wind speed measurements in a 1 day window before the ICME/disturbance arrival time at 1 AU, and its standard deviation was used for the error bars.

Most ICME speeds at 1 AU are larger than the ambient solar wind speed, which can be seen on the x axis in Figure 4. Slightly different from previous findings, \bar{v} (the average transit speed between 1 AU and Mars) is generally smaller than $v_{1 \text{ AU}}$ (which corresponds to a deceleration of the ICME), as visible on the y axis, apart from 3 cases where the error bars are also very large. Our results tend to show that lower ambient solar wind speeds compared to the ICME speed generally result in more deceleration even beyond 1 AU, as expected.

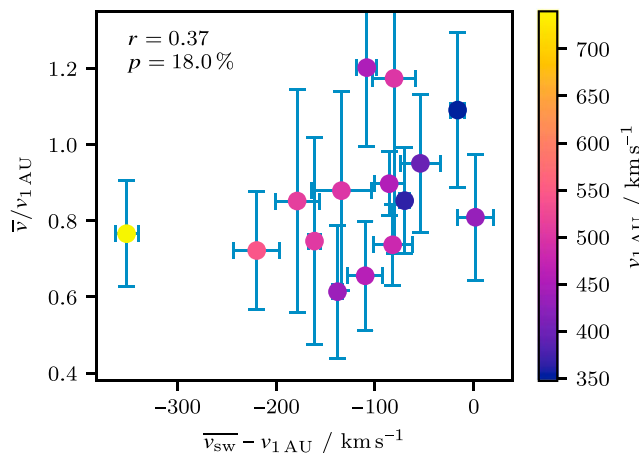


Figure 4. Comparison of the ratio $\bar{v}/v_{1 \text{ AU}}$ to $v_{\text{sw}} - v_{1 \text{ AU}}$, where v_{sw} is the ambient solar wind speed measured at ACE. The colors show the initial speed of the ICME at $v_{1 \text{ AU}}$. The Pearson correlation coefficient r and the probability p that such a data set was produced by an uncorrelated system are displayed in the plot.

However, there is a considerable amount of variance in the data points, which is reflected by the Pearson correlation coefficient $r = 0.37$ in Figure 4 not being very high. This variance can possibly be due to the determined speed \bar{v} being influenced by the geometry of the ICME: In general, the propagation of different parts of the ICME can be affected differently by ambient solar wind conditions and the interaction with other structures, such as stream interaction regions (SIRs)/corotating interaction regions (CIRs) and other ICMEs, potentially resulting in a variation of the ICMEs' geometric shape. This could lead to a radial asymmetry of the ICME resulting in larger uncertainties in our analysis especially when the two observers have a bigger longitudinal separation. A demonstration of this influence is also shown as a cartoon in Figure 5, together with an example of the ENLIL model result in Figure 6 (explained later in section 3.3) for ICME 11 where we suspect that this effect led to the ratio $\bar{v}/v_{1 \text{ AU}}$ being 1.20 ± 0.21 . Another example is visible in Figure 9, where ICME 12 is merging with an SIR structure, possibly leading to a slight "acceleration," $\bar{v}/v_{1 \text{ AU}} = 1.17 \pm 0.46$. Similar effects have been observed previously by Prise et al. (2015) and Winslow et al. (2016).

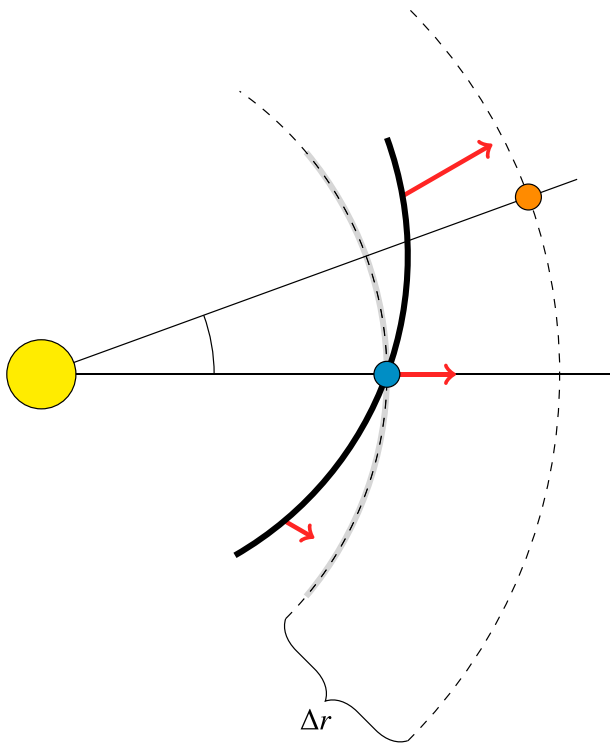


Figure 5. Cartoon illustration of the possible influence of the ICME shape on the measured speeds when the two observation locations are not perfectly aligned in their heliospheric longitudes. In this case, the inclined shape causes a perceived “speedup” of the ICME between Earth and Mars even if the actual speed of the ICME stays constant.

Another comparison can be made to the mean acceleration values that we calculated for the travel between $21.5 R_{\odot}$ and 1 AU ($a_{\text{Sun}, 1 \text{ AU}}$) and between 1 AU and Mars ($a_{1 \text{ AU}, \text{ Mars}}$) as shown in Figure 7. The acceleration was calculated using equation (4), which depends on T_{correl}^2 , amplifying the error bars. The big variations of a shown in the figure indicate that ICMEs are very dynamic and their propagation depends on various properties, such as the different ambient solar wind conditions at different parts of the ICME and the interaction with other heliospheric structures. Our results suggest that the dynamics of the propagation continue to evolve beyond 1 AU and that, although the acceleration values up to and after 1 AU tend to be related (supported by a Pearson correlation coefficient of $r = 0.29$), the acceleration is hardly a constant value. This is because (a) the ambient environment that the ICME travels through fluctuates due to the time-varying structures of the heliosphere (as shown, e.g., by Temmer et al., 2011) and (b) the ambient solar wind conditions vary throughout the heliosphere, thus diversely affecting the same ICME at different locations.

We have also marked the four quadrants in the plot, showing which ICMEs kept decelerating before and after 1 AU (lower left quadrant) and which changed from acceleration to deceleration (lower right) or the other way round (upper left). There are no ICMEs that accelerated before and after 1 AU (upper right quadrant), and two cases that “accelerated” between 1 AU and Mars were addressed above (events 11 and 12). There are also two ICMEs that seem to have accelerated between the Sun and 1 AU, that is, event numbers 10 and 15, which have very low launch speeds reported (below 400 km s^{-1} in the DONKI list, as well as even lower values in the SOHO/LASCO and CACTus (Computer Aided CME Tracking) databases). These could of course be physical but might also be due to the projection effect used in the image-based remote sensing analysis used to derive the launch speed. As the current paper is not focusing on the launch properties of the CMEs we did not pursue this matter further.

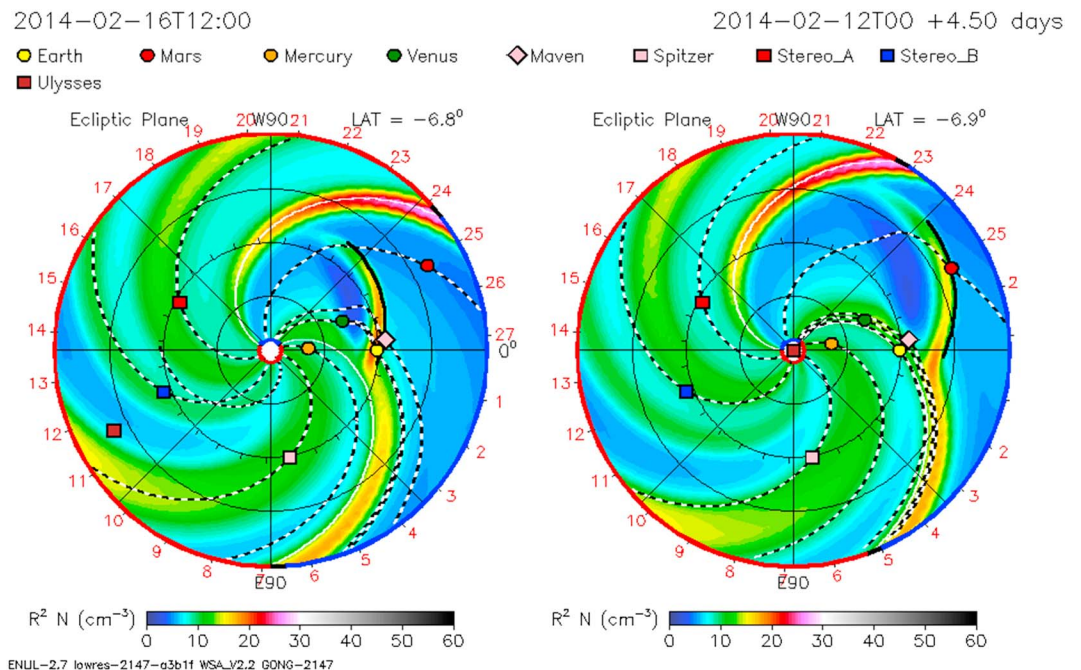


Figure 6. ENLIL simulation for the 15 February 2014 ICME, showing the same effect that was illustrated in Figure 5 (left, arrival at Earth; right, arrival at Mars). The CME front was emphasized manually using a black line.

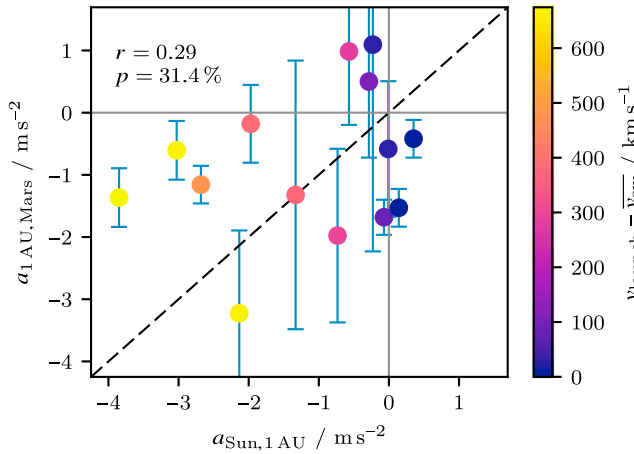


Figure 7. Comparison of the acceleration $a_{\text{Sun}, 1 \text{ AU}}$ between $21.5 R_{\odot}$ and the arrival at 1 AU and $a_{1 \text{ AU}, \text{ Mars}}$ between the arrival at 1 AU and the arrival at Mars. The Pearson correlation coefficient r and the probability p that such a data set was produced by an uncorrelated system are displayed in the plot. The diagonal line marks where the accelerations would be equal, and the gray lines divide the four quadrants of the plot.

In Figure 8, we correlated the acceleration between the Sun and 1 AU with the launch speed (left) and the acceleration between 1 AU and Mars with the speed at 1 AU (right). Both plots show that a stronger deceleration is correlated with higher ICME speeds, which is supported by high Pearson correlation coefficients of $r = -0.94$ and -0.64 and low corresponding probabilities $p = 0.0\%$ and 1.5% for uncorrelated data, respectively. Again, the error bars in Figure 8 (right) are large due to the dependence of a on T_{correl}^2 . Comparing our results for the acceleration with the values that Richardson (2014) obtained for ICMEs propagating from Earth to the Ulysses spacecraft (shown in their Figure 22 in a similar manner as our Figure 8), which was at a distance of between 3.74 and 5.41 AU from the Sun at that time, we find that our average deceleration value of $(0.81 \pm 0.33) \text{ m s}^{-2}$ is much larger than their values of up to 0.1 m s^{-2} . This suggests that the deceleration becomes weaker at a larger radial distance beyond Mars, thus resulting in a lower average value between Earth and Ulysses.

3.3. WSA-ENLIL+Cone Model

The Wang-Sheeley-Arge (WSA) ENLIL model (Odstrcil et al., 2004) is a widely used tool to predict solar wind propagation in the heliosphere. It is based on an MHD simulation and can be combined with a cone model to

describe the propagation of ICMEs. Using the *Space Weather Database of Notifications, Knowledge, Information* (DONKI, <https://kauai.ccmc.gsfc.nasa.gov/DONKI/>), which is based on coronagraph observations of CMEs close to their launch from the Sun, we matched most of the ICMEs in our study to WSA-ENLIL+Cone model simulation results provided by the Community Coordinated Modeling Center (CCMC) (<https://ccmc.gsfc.nasa.gov/missionsupport/>). In some cases, there are multiple ENLIL results for the same ICME (using slightly different input parameters)—in that situation, we chose the one that gave the best 1 AU arrival time compared to the observations from the Richardson and Cane or Jian lists, respectively. In one case (ICME 14 in Table 3), we did not find any event output in the DONKI database that would possibly match the observed arrival time at 1 AU. Figure 9 shows a graphical representation of an ENLIL simulation result, specifically the ICME arriving at Earth on 5 April 2014 and at Mars on 7 April 2014, respectively (ICME 12 in Table 3).

To compare our measured ICME traveltimes to the ENLIL model results, we applied the cross-correlation method described in section 2.3 to the plasma number density n at Earth (or STEREO) and Mars obtained from the model. This gives us another time lag value, which is considered to be the traveltime that the ENLIL model predicts. In most cases, due to the smooth nature of the simulated data, the uncertainty of the traveltime is smaller than for the one obtained from measured Forbush decreases.

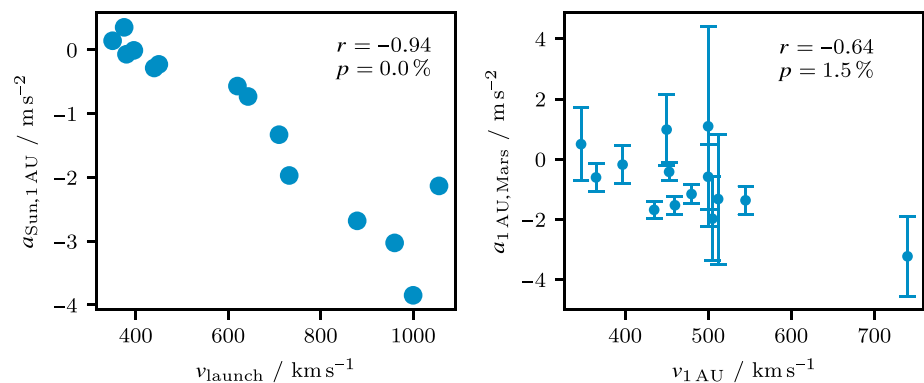


Figure 8. Comparison of the (right) acceleration $a_{1 \text{ AU}, \text{ Mars}}$ between the arrival at 1 AU and the arrival at Mars with the speed $v_{1 \text{ AU}}$ and the (left) acceleration $a_{\text{Sun}, 1 \text{ AU}}$ between $21.5 R_{\odot}$ and the arrival at 1 AU with the speed v_{launch} of the ICME at $21.5 R_{\odot}$. The Pearson correlation coefficients r and the probabilities p that such data sets were produced by an uncorrelated system are displayed in the plots.

Table 3*Table of All the ICMEs Examined in This Study*

ICME	Obs S/C	Repetition from Table 2		Acceleration		Model input and results			
		$t_{1 \text{ AU}}$ (UTC)	T_{correl} /days	$a_{1 \text{ AU, Mars}}$ /m s ⁻²	$a_{\text{Sun, 1 AU}}$ /m s ⁻²	$t_{21.5 R_{\odot}}$ (UTC)	T_{ENLIL} /days	T_{DBM} /days	$\Gamma_{\odot-1 \text{ AU}}$ /10 ⁻⁷ km ⁻¹
1	STB	2012-9-25 16:26	1.24±0.23	-3.2±1.3	-2.13	2012-9-23 18:58	1.03±0.14	1.0	0.082±0.004
2	STB	2012-10-17 06:57	2.05±0.33	-0.60±0.47	-3.03	2012-10-14 08:45	1.54±0.26	2.1	0.224±0.006
3	STB	2012-10-25 19:10	2.31±0.66	-1.68±0.28	-0.07	2012-10-21 03:59	1.28±0.34	2.5	0.058±0.006
4	STB	2012-11-11 13:36	1.33±0.46	-1.3±2.2	-1.33	2012-11-8 07:21	1.33±0.23	1.8	0.17±0.03
5	STB	2012-11-19 09:50	1.50±0.54	-2.0±1.4	-0.73	2012-11-16 06:32	0.94±0.19	1.7	0.138±0.007
6	STB	2012-11-28 03:36	1.46±0.27	0.5±1.2	-0.29	2012-11-23 17:17	1.46±0.28	1.6	0.7±0.2
7	STA	2013-5-29 12:20	2.53±0.37	-1.16±0.30	-2.68	2013-05-26 22:58	1.37±0.25	1.9	0.34±0.05
8	STA	2013-6-27 16:17	2.53±0.48	-0.18±0.63	-1.97	2013-6-24 08:08	1.97±0.41	2.6	0.40±0.07
9	STA	2013-7-25 06:12	2.57±0.56	-1.37±0.47	-3.85	2013-7-22 09:55	1.97±0.44	2.1	0.19±0.02
10	STA	2013-8-10 15:00	2.57±0.24	-0.42±0.30	0.35	2013-8-7 02:53	2.57±0.26	2.4	-2±1
11	EARTH	2014-2-15 13:45	2.14±0.37	1.0±1.2	-0.57	2014-2-12 18:51	2.01±0.32	2.6	0.15±0.02
12	EARTH	2014-4-5 19:00	1.84±0.72	1.1±3.3	-0.23	2014-4-2 00:19	2.53±0.30	2.4	0.7±0.6
13	EARTH	2014-4-18 19:00	2.40±0.71	-0.6±1.1	-0.01	2014-4-14 19:44	2.35±0.23	2.2	0.01±0.01
14	EARTH	2016-3-20 07:00	3.00±0.61	-0.63±0.42				3.0	
15	EARTH	2016-8-2 14:00	2.40±0.53	-1.53±0.30	0.14	2016-7-29 08:50	2.31±0.24	3.1	-0.5±0.3
Average			2.12±0.13	-0.81±0.33	-1.17		1.76±0.08	2.2	0.13
				$\sigma = 1.11$	$\sigma = 1.29$				

Note. This table supplements the data from Table 2 with the average acceleration values calculated using equation (4), the time $t_{21.5 R_{\odot}}$ used for the ENLIL simulations, the traveltime T_{ENLIL} calculated from the ENLIL model results and the traveltime T_{DBM} calculated using DBM by propagating the ICME from 1 AU to Mars (section 3.3) using a drag parameter of $\Gamma = 0.1 \times 10^{-7} \text{ km}^{-1}$. The last column shows an estimation of the actual drag parameter for this event between the Sun and 1 AU calculated using the observation values as described at the end of section 3.4, where the average displayed in the bottom row is weighted using the inverse errors. The acceleration values of events 10 and 15 are very small with absolute errors similar to the others, which makes the errors of Γ large. However, due to the weighted mean calculation, these two values only have a very small influence on the mean Γ value for all events shown in the last row. Γ values for the propagation between 1 AU and Mars are not shown; their uncertainties are so large that the values are not meaningful. For Event 15, there is a negative Γ value because the speed at 1 AU is larger than the launch speed, which is very low both in the DONKI and CACTUS ICME catalogs. Dates are formatted as year/month/day.

In Figure 10 (top left), we compare the traveltimes calculated by the ENLIL model with the ones obtained from the in situ data in this work. Both traveltimes are also listed in Tables 2 and 3. For many events, ENLIL seems to predict a slightly faster propagation. Results for faster ICMEs (e.g., the 28 November 2012 ICME at STEREO B—ICME 6 in Tables 2 and 3) seem to agree quite well, while the slower events show larger differences. This might be the result of slower ICMEs being exposed to the disturbances in the interplanetary space for a longer time, thus accumulating a larger amount of possible uncertainties in the model. However, a more systematic statistical study based on more events should be carried out in the future to draw a solid statement on this matter.

We also calculated the mean difference between the results

$$\langle T_{\text{ENLIL}} - T_{\text{correl}} \rangle = -7 \pm 11 \text{ h}$$

and the average absolute difference

$$\langle |T_{\text{ENLIL}} - T_{\text{correl}}| \rangle \approx 10 \text{ h}.$$

The error given here is the standard error of the mean, not the standard deviation.

3.4. Drag-Based Model

A simpler model for the propagation of ICMEs is the Drag-Based Model (DBM), described in Vršnak et al. (2013) and Žic et al. (2015). The DBM is based on the assumption that beyond a distance of approximately $20 R_{\odot}$, the dominating influence on ICMEs is an “aerodynamic” drag force with an empirically determined drag

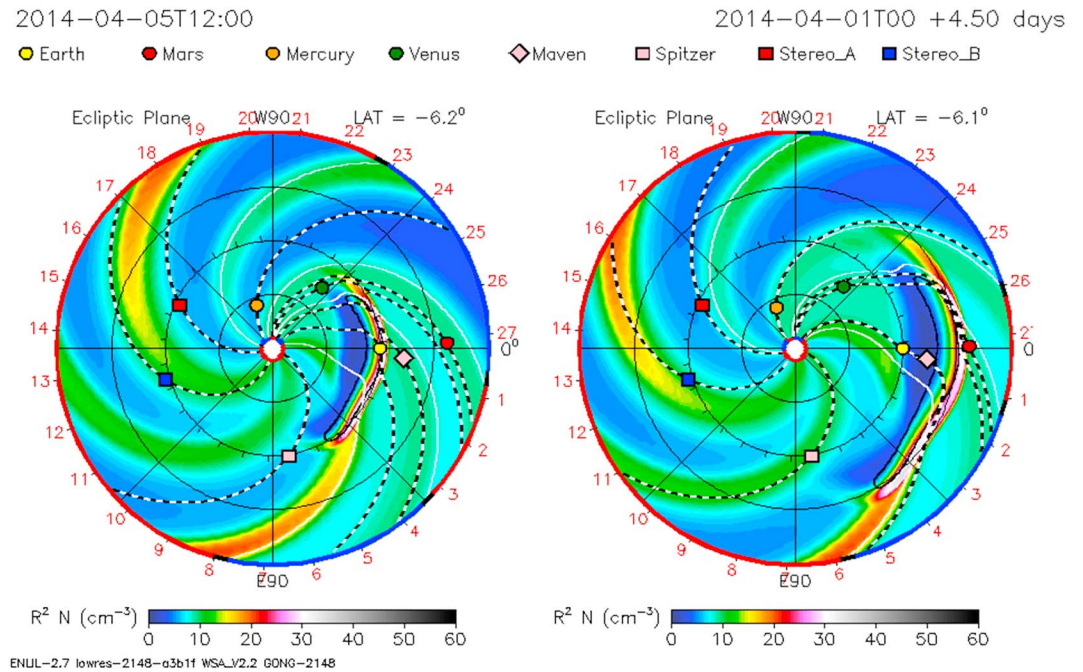


Figure 9. Example of an ENLIL simulation result for the 5 April 2014 ICME (left, arrival at Earth; right, arrival at Mars).

parameter Γ . The main difference between DBM and ENLIL is that the former does not employ numerical MHD simulations—the drag equations can be solved analytically. Therefore, the simulation is computationally inexpensive.

Vršnak et al. (2014) already compared results from DBM and ENLIL simulations and found that the ICME arrival times at Earth predicted by the two models generally agree quite well with average absolute-value difference of below 8 h. For these results, drag parameter values between $\Gamma = 0.1 \times 10^{-7}$ and $0.2 \times 10^{-7} \text{ km}^{-1}$ and solar wind speeds between $w = 400$ and 500 km s^{-1} were used as an input for the DBM.

We apply the DBM model in such a way that the propagation of ICMEs is simulated starting from 1 AU, where the in situ measurement of the ICME is used as input, thus avoiding the uncertainty of the propagation from the Sun up to 1 AU. As the input for DBM, we used the local ICME speed ($v_{1 \text{ AU}}$) and the ambient solar wind speed for each event measured at ACE or STEREO as described in section 3.1. The drag parameter Γ was chosen to be $0.1 \times 10^{-7} \text{ km}^{-1}$, which is a low value that is commonly used for describing the propagation of the interplanetary shock associated with an ICME. We chose this value because the shock is related to the first step of the Forbush decrease (e.g., Cane, 2000). Assuming that the ICME propagates outward radially, the ICMEs' half widths and the heliospheric longitudes of their propagation directions were taken from the DONKI database entries, as previously done for the ENLIL model (as such information is not available at 1 AU).

The arrival times at Mars predicted by DBM are marked in Figure 2 as well as Figures A1–A5 in Appendix A. Additionally, Figure 10 (top right) compares the traveltimes predicted by DBM to the results of the correlation method, and Figure 10 (top left) compares the two models, ENLIL and DBM.

The mean difference and mean absolute difference between the results are the following:

$$\begin{aligned} \langle T_{\text{DBM}} - T_{\text{correl}} \rangle &= (1 \pm 9) \text{ h} \\ \langle |T_{\text{DBM}} - T_{\text{correl}}| \rangle &\approx (7) \text{ h} \\ \langle T_{\text{DBM}} - T_{\text{ENLIL}} \rangle &= (9 \pm 10) \text{ h} \\ \langle |T_{\text{DBM}} - T_{\text{ENLIL}}| \rangle &\approx 11 \text{ h}. \end{aligned}$$

On average, DBM gives slightly better results than ENLIL for these events, even though the amount of variance is similar. Probably, this is primarily due to the fact that we could use DBM for propagation from 1 AU to Mars instead of from the Sun.

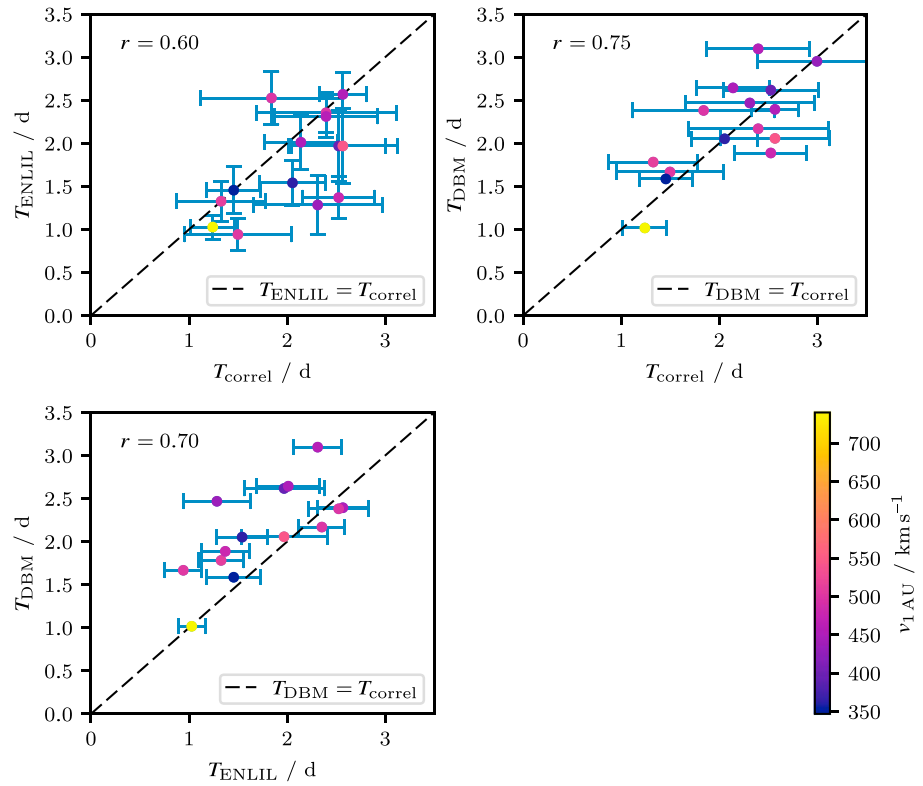


Figure 10. Plots comparing the ICME traveltimes between 1 AU and Mars determined using the cross-correlation method and calculated by ENLIL or DBM. The diagonal line marks where the traveltimes would be equal. The Pearson correlation coefficient r is noted in the top left corner.

The agreement between the DBM and ENLIL models is similar to the one of ENLIL, and the correlation method results with an average absolute-value difference slightly above the value of 8 h determined by Vršnak et al. (2014) for the propagation up to 1 AU. This difference seems reasonable as the propagation from the Sun out to Mars (~ 1.5 AU) takes a longer time and can therefore introduce a larger amount of error.

Under the assumption that the acceleration a of an ICME stays constant between the Sun and 1 AU and between 1 AU and Mars and with a simplified, one-dimensional version of DBM (disregarding the influence of the geometric shape of the ICME), we also tried to derive the actual values of the drag parameter Γ based on the observations and our calculated a values by solving the following equation (cf. Vršnak et al., 2013, equation (1))

$$a = -\Gamma(v_{\text{ICME}} - v_{\text{sw}})|v_{\text{ICME}} - v_{\text{sw}}| \quad (5)$$

for Γ .

Using the average speed $v_{\text{ICME}} = (v_{\text{launch}} + v_{1 \text{ AU}})/2$ and $a = a_{\text{Sun}, 1 \text{ AU}}$ (from Table 2), we get an estimation of Γ between the Sun and 1 AU, which is given in Table 3. By calculating a weighted average using the inverse errors of these Γ values, we obtain a result of $0.09 \times 10^{-7} \text{ km}^{-1}$, which shows that our assumption of $\Gamma = 0.1 \times 10^{-7} \text{ km}^{-1}$ was reasonable. Nonetheless, we note that the variance of Γ for different events is considerable, which reflects the dynamic and variant nature of ICMEs and suggests that the approximated constant value of Γ in DBM may result in uncertainties in the modelling procedure. The same Γ values could also be calculated between 1 AU and Mars using $v_{\text{ICME}} = \bar{v}$ and $a = a_{1 \text{ AU}, \text{ Mars}}$; however, the results have propagated uncertainties that are too large to be meaningful.

4. Conclusion

We have described a method to determine the traveltime of ICMEs between two heliospheric locations using the cross-correlation function of two in situ data sets and applied it to 15 ICMEs and their Forbush decreases

observed at Earth or the STEREO spacecraft and Mars close to their oppositions between 2012 and 2016. The method gives meaningful results in most cases apart from periods when ICMEs interact with each other and/or with SIRs/CIRs.

The results were used as the basis for this first statistical study of ICME-caused FDs observed at both 1 AU and 1.5 AU. It was found that the average ICME in our sample slightly decelerated during its propagation between 1 AU and 1.5 AU. Additionally, the results support that slower ambient solar wind speeds in comparison to the maximum ICME speed lead to a larger amount of deceleration. More studies based on a higher number of events in the future would help to better quantify these results.

The traveltimes between 1 AU and Mars obtained for the 15 events were compared with results from the ENLIL and DBM models. To derive traveltimes from the interplanetary plasma number density data output by ENLIL for different locations, the same cross-correlation method was used. On average, ENLIL predicts a faster propagation from 1 AU to Mars, but the ENLIL results seem to be less accurate for slower ICMEs in the study, which might be an effect of accumulation of uncertainties during the longer traveltime.

Additionally, the observations were compared to results from the Drag-Based Model. Unlike ENLIL, we could use the observations at 1 AU as the basis for DBM and simulate the propagation from 1 AU to Mars. Avoiding the uncertainties of the propagation close to the Sun, this led to a slightly better agreement with the observations at Mars.

This highlights the importance of space weather modeling taking into account not only information about the launch of CMEs at the Sun but also the in situ measurements farther away, for example, at 1 AU, to improve forecasts for space weather hazards for robotic missions positioned beyond 1 AU. With future missions, such as Solar Orbiter and the Parker Solar Probe, we will have more measurements available at solar distances of less than 0.3 AU, which should be exploited as an input for modeling of space weather scenarios.

Appendix A: Cross-Correlation Analysis Plots for Each Event

The results based on the cross-correlation method for all the ICMEs in this study are presented in this appendix.

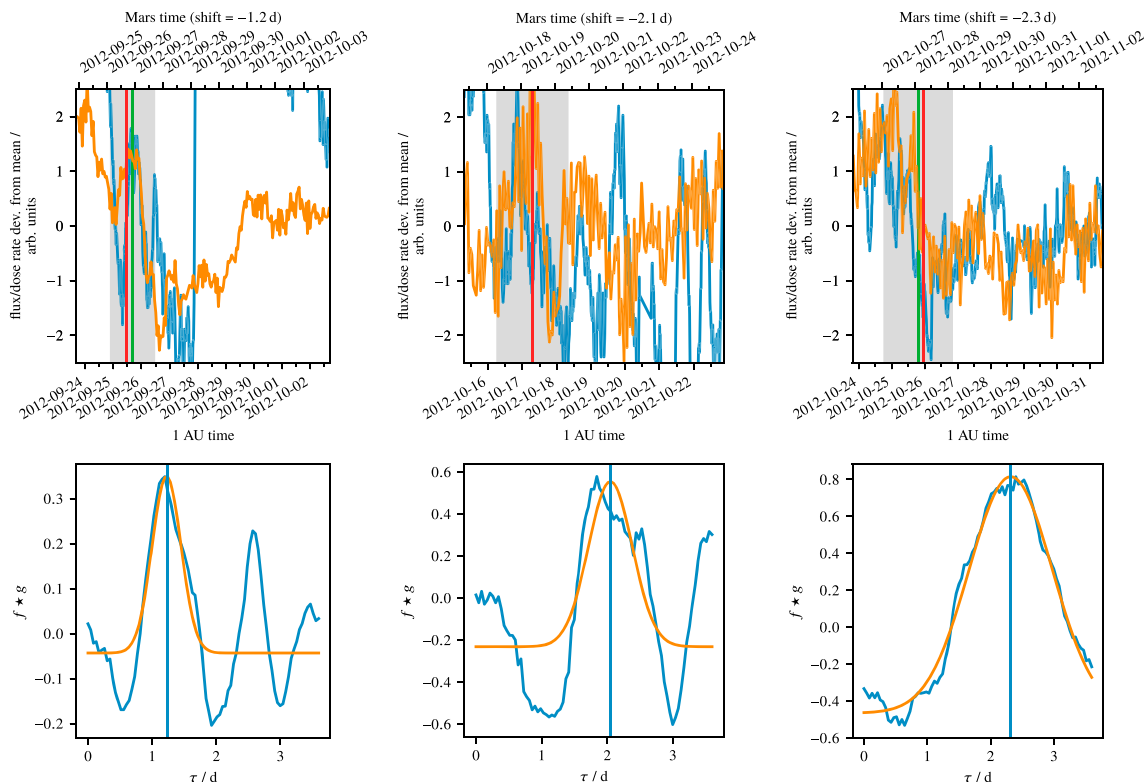


Figure A1. Plots showing the application of the cross-correlation method to every single ICME in the study. These are Events 1 to 3 (all observed at STEREO B and Mars). The legend for the plots is in Figure 2.

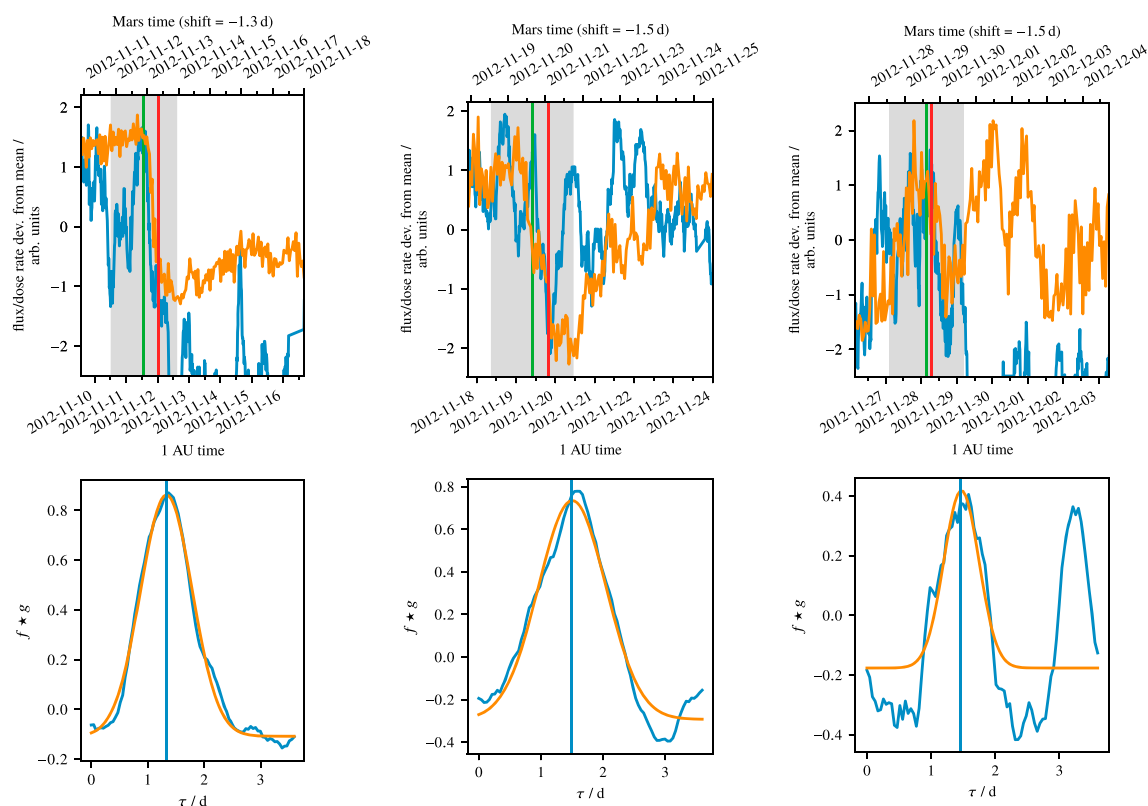


Figure A2. Plots showing the application of the cross-correlation method to every single ICME in the study. These are Events 4 to 6 (all observed at STEREO B and Mars). The legend for the plots is in Figure 2.

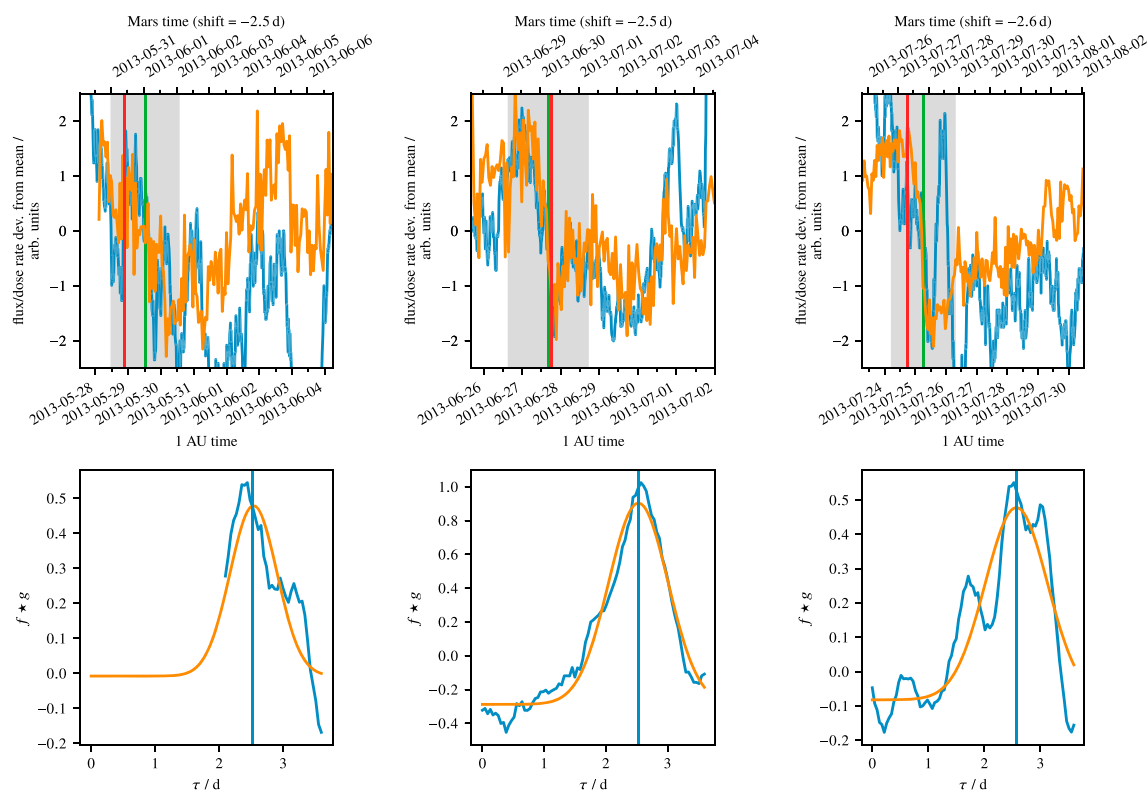


Figure A3. Plots showing the application of the cross-correlation method to every single ICME in the study. These are Events 7 to 9 (all observed at STEREO A and Mars). The legend for the plots is in Figure 2.

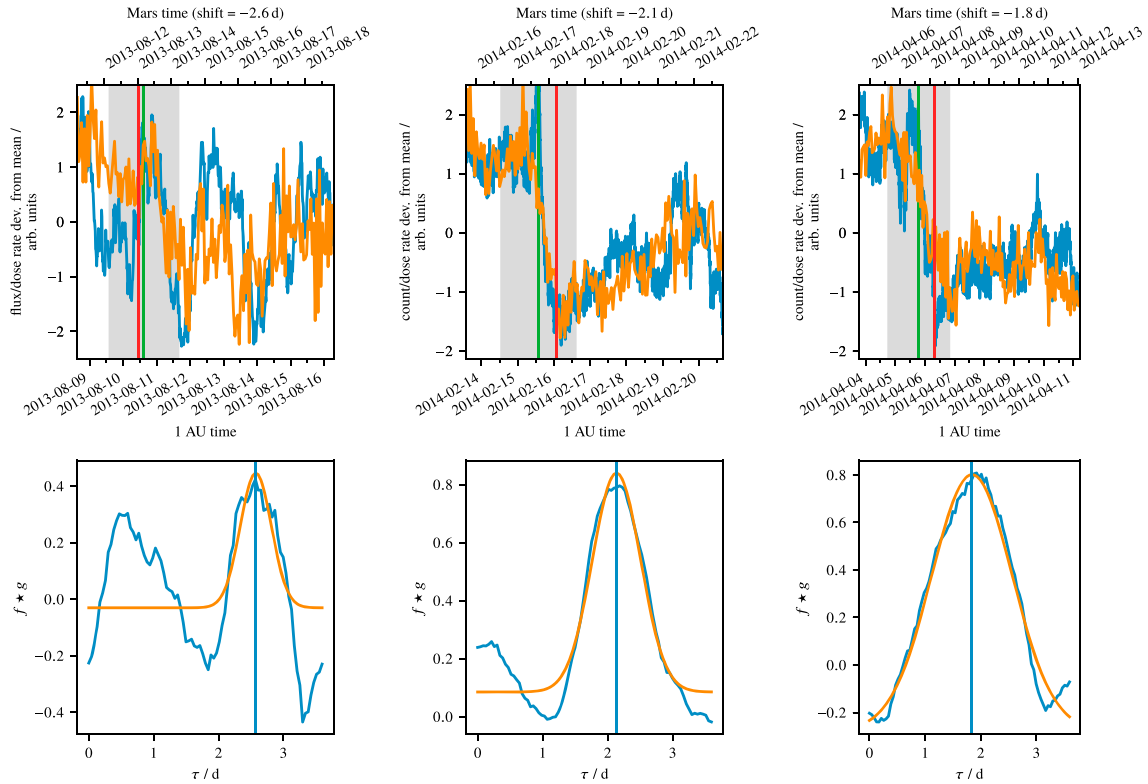


Figure A4. Plots showing the application of the cross-correlation method to every single ICME in the study. These are Events 10 (observed at STEREO A and Mars), 11, and 12 (observed at Earth and Mars).

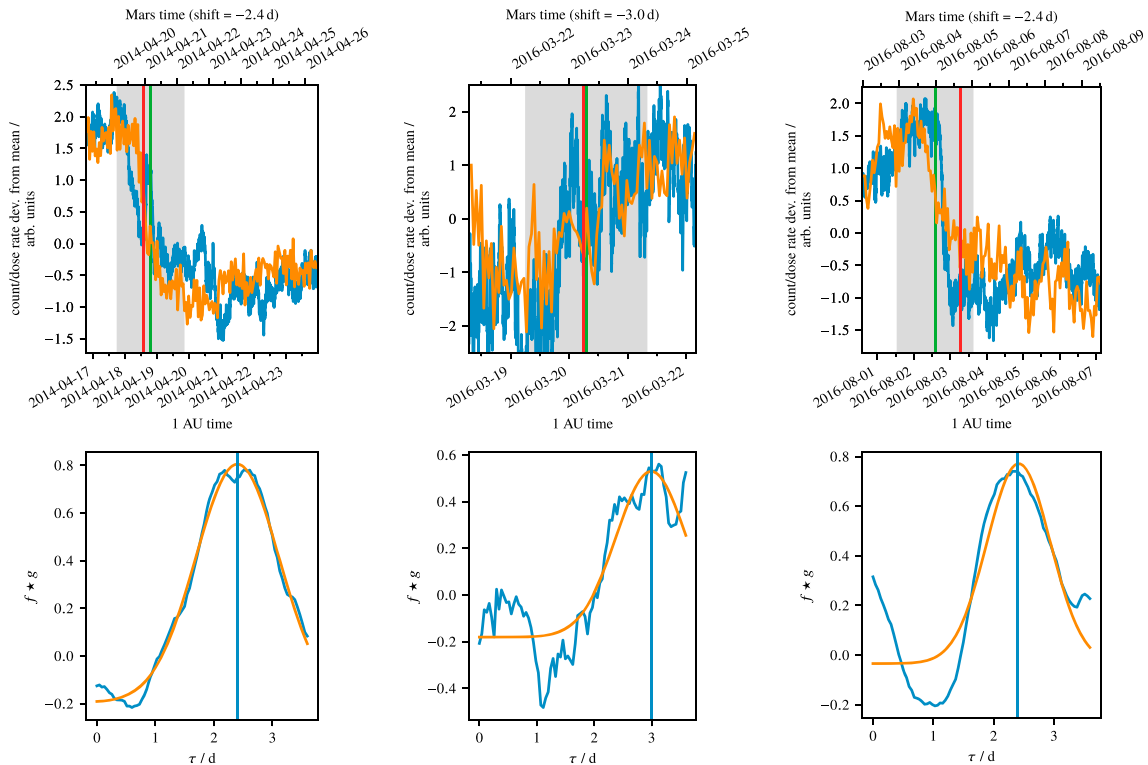


Figure A5. Plots showing the application of the cross-correlation method to every single ICME in the study. These are Events 13 to 15 (all observed at Earth and Mars). The legend for the plots is in Figure 2.

Acknowledgments

RAD is supported by NASA (HEOMD) under JPL subcontract 1273039 to Southwest Research Institute and in Germany by DLR and DLR's Space Administration grants 50QM0501, 50QM1201, and 50QM1701 to the Christian Albrechts University, Kiel. Jingnan Guo and Robert Wimmer-Schweingruber acknowledge stimulating discussions with the ISSI team "Radiation Interactions at Planetary Bodies" and thank ISSI for its hospitality. The research leading to these results has received funding from the European Union's Horizon 2020 research and innovation programme under the Marie Skłodowska-Curie grant agreement 745782. Lan K. Jian is supported by NSF grants AGS 1259549 and 1321493. Bojan Vršnak, Jaša Čalোগović and Mateja Dumbović acknowledge financial support by the Croatian Science Foundation under project 6212 "Solar and Stellar Variability". We acknowledge the NMDB database (www.nmdb.eu), funded under the European Union's FP7 Programme (contract 213007), for providing data. The data from South Pole neutron monitor is provided by the University of Delaware with support from the U.S. National Science Foundation under grant ANT-0838839. Simulation results have been provided by the Community Coordinated Modeling Center at Goddard Space Flight Center through their archive of real-time simulations (<http://ccmc.gsfc.nasa.gov/missionsupport>). The CCMC is a multiagency partnership between NASA, AFMC, AFOSR, AFRL, AFWA, NOAA, NSF, and ONR. ENLIL with Cone Model was developed by D. Odstrčil at George Mason University. We thank the ACE SWEPAM instrument team and the ACE Science Center for providing the ACE data. We acknowledge the STEREO IMPACT and PLASTIC teams (NASA contracts NAS5-00132 and NAS5-00133) for the use of the solar wind plasma and magnetic field data.

References

- Burlaga, L. F., McDonald, F. B., Goldstein, M. L., & Lazarus, A. J. (1985). Cosmic ray modulation and turbulent interaction regions near 11 AU. *Journal of Geophysical Research*, 90, 12,027–12,039. <https://doi.org/10.1029/JA090iA12p12027>
- Cane, H. V. (2000). Coronal mass ejections and Forbush decreases. *Space Science Reviews*, 93(1), 55–77. <https://doi.org/10.1023/A:1026532125747>
- Ehresmann, B., Zeitlin, C., Hassler, D. M., Wimmer-Schweingruber, R. F., Böhm, E., & Böttcher, S. (2014). Charged particle spectra obtained with the Mars Science Laboratory Radiation Assessment Detector (MSL/RAD) on the surface of Mars. *Journal of Geophysical Research: Planets*, 119, 468–479. <https://doi.org/10.1002/2013JE004547>
- Forbush, S. E. (1937). On the effects in cosmic-ray intensity observed during the recent magnetic storm. *Physical Review*, 51, 1108–1109. <https://doi.org/10.1103/PhysRev.51.1108.3>
- Galvin, A. B., Kistler, L. M., Popecki, M. A., Farrugia, C. J., Simunac, K. D. C., Ellis, L., ... Steinfeld, D. (2008). The Plasma and Suprathermal Ion Composition (PLASTIC) investigation on the STEREO observatories. *Space Science Reviews*, 136(1), 437–486. <https://doi.org/10.1007/s11214-007-9296-x>
- Gopalswamy, N., Lara, A., Yashiro, S., Kaiser, M. L., & Howard, R. A. (2001). Predicting the 1-AU arrival times of coronal mass ejections. *Journal of Geophysical Research*, 106(A12), 29,207–29,217. <https://doi.org/10.1029/2001JA000177>
- Grotzinger, J. P., Crisp, J., Vasavada, A. R., Anderson, R. C., Baker, C. J., Barry, R., ... Wiens, R. C. (2012). Mars Science Laboratory mission and science investigation. *Space Science Reviews*, 170(1), 5–56. <https://doi.org/10.1007/s11214-012-9892-2>
- Guo, J., Zeitlin, C., Wimmer-Schweingruber, R. F., Rafkin, S., Hassler, D. M., & Posner, A. (2015). Modeling the variations of dose rate measured by RAD during the first MSL Martian year: 2012–2014. *The Astrophysical Journal*, 810(1), 24.
- Guo, J., Lillis, R., Wimmer-Schweingruber, R. F., Zeitlin, C., Simonson, P., Rahmati, A., ... Böttcher, S. (2017). Measurements of Forbush decreases at Mars: Both by MSL on ground and by MAVEN in orbit. *Astronomy and Astrophysics*, 1–15. <https://doi.org/10.1051/0004-6361/201732087>
- Guo, J., Slaba, T. C., Zeitlin, C., Wimmer-Schweingruber, R. F., Badavi, F. F., Böhm, E., ... Rafkin, S. (2017). Dependence of the Martian radiation environment on atmospheric depth: Modeling and measurement. *Journal of Geophysical Research: Planets*, 122, 329–341. <https://doi.org/10.1002/2016JE005206>
- Hassler, D. M., Zeitlin, C., Wimmer-Schweingruber, R. F., Böttcher, S., Martin, C., Andrews, J., ... Cucinotta, F. A. (2012). The radiation assessment detector (RAD) investigation. *Space Science Reviews*, 170(1), 503–558. <https://doi.org/10.1007/s11214-012-9913-1>
- Hassler, D. M., Zeitlin, C., Wimmer-Schweingruber, R. F., Ehresmann, B., Rafkin, S., & Eigenbrode, J. L. (2014). Mars' surface radiation environment measured with the Mars Science Laboratory's Curiosity rover. *Science*, 343(6169), 1244797.
- Hess, V. F., & Demmelair, A. (1937). World-wide effect in cosmic ray intensity, as observed during a recent magnetic storm. *Nature*, 140, 316–317. <https://doi.org/10.1038/140316a0>
- Jian, L. K., Russell, C. T., Luhmann, J. G., Skoug, R. M., & Steinberg, J. T. (2008). Stream interactions and interplanetary coronal mass ejections at 5.3 AU near the solar ecliptic plane. *Solar Physics*, 250(2), 375–402. <https://doi.org/10.1007/s11207-008-9204-x>
- Jian, L. K., Russell, C. T., Luhmann, J. G., Galvin, A. B., & Simunac, K. D. C. (2013). Solar wind observations at STEREO: 2007–2011. *AIP Conference Proceedings*, 1539(1), 191–194. <https://doi.org/10.1063/1.4811020>
- Jordan, A. P., Spence, H. E., Blake, J. B., & Shaul, D. N. A. (2011). Revisiting two-step Forbush decreases. *Journal of Geophysical Research*, 116, A11103. <https://doi.org/10.1029/2011JA016791>
- Kumar, A., & Badruddin (2014). Interplanetary coronal mass ejections, associated features, and transient modulation of galactic cosmic rays. *Solar Physics*, 289(6), 2177–2205. <https://doi.org/10.1007/s11207-013-0465-7>
- Köhler, J., Zeitlin, C., Ehresmann, B., Wimmer-Schweingruber, R. F., Hassler, D. M., Reitz, G., ... Kortmann, O. (2014). Measurements of the neutron spectrum on the Martian surface with MSL/RAD. *Journal of Geophysical Research: Planets*, 119, 594–603. <https://doi.org/10.1002/2013JE004539>
- Liu, Y., Davies, J. A., Luhmann, J. G., Vourlidas, A., Bale, S. D., & Lin, R. P. (2010). Geometric triangulation of imaging observations to track coronal mass ejections continuously out to 1 AU. *The Astrophysical Journal Letters*, 710(1), L82.
- Liu, Y. D., Richardson, J. D., Wang, C., & Luhmann, J. G. (2014). Propagation of the 2012 March coronal mass ejections from the Sun to heliopause. *The Astrophysical Journal Letters*, 788(2), L28.
- Lockwood, J. A. (1971). Forbush decreases in the cosmic radiation. *Space Science Reviews*, 12(5), 658–715. <https://doi.org/10.1007/BF00173346>
- Lugaz, N., Farrugia, C. J., Davies, J. A., Möstl, C., Davis, C. J., Rousset, I. I., & Temmer, M. (2012). The deflection of the two interacting coronal mass ejections of 2010 May 23–24 as revealed by combined in situ measurements and heliospheric imaging. *The Astrophysical Journal*, 759(1), 68.
- Maričić, D., Vršnak, B., Dumbović, M., Žic, T., Roša, D., Hržina, D., ... Mujić, N. (2014). Kinematics of interacting ICMEs and related Forbush decrease: Case study. *Solar Physics*, 289(1), 351–368. <https://doi.org/10.1007/s11207-013-0314-8>
- Masías-Meza, J. J., Dasso, S., Démoulin, P., Rodriguez, L., & Janvier, M. (2016). Superposed epoch study of ICME sub-structures near Earth and their effects on galactic cosmic rays. *Astronomy and Astrophysics*, 592, A118. <https://doi.org/10.1051/0004-6361/201628571>
- McComas, D., Bame, S., Barker, P., Feldman, W., Phillips, J., Riley, P., & Griffiee, J. (1998). Solar wind electron proton alpha monitor (SWEPAM) for the Advanced Composition Explorer. *Space Science Reviews*, 86(1), 563–612. <https://doi.org/10.1023/A:1005040232597>
- Möstl, C., Amla, K., Hall, J. R., Liewer, P. C., Jong, E. M. D., Colaninno, R. C., ... Galvin, A. B. (2014). Connecting speeds, directions and arrival times of 22 coronal mass ejections from the Sun to 1 AU. *The Astrophysical Journal*, 787(2), 119.
- Odstrčil, D., Riley, P., & Zhao, X. P. (2004). Numerical simulation of the 12 May 1997 interplanetary CME event. *Journal of Geophysical Research*, 109, A02116. <https://doi.org/10.1029/2003JA010135>
- Parks, T. W., & Burrus, C. S. (1987). *Digital filter design*. New York: Wiley-Interscience.
- Prise, A. J., Harra, L. K., Matthews, S. A., Arridge, C. S., & Achilleos, N. (2015). Analysis of a coronal mass ejection and corotating interaction region as they travel from the Sun passing Venus, Earth, Mars, and Saturn. *Journal of Geophysical Research: Space Physics*, 120, 1566–1588. <https://doi.org/10.1002/2014JA020256>
- Rafkin, S. C. R., Zeitlin, C., Ehresmann, B., Hassler, D., Guo, J., Köhler, J., ... The MSL Science Team (2014). Diurnal variations of energetic particle radiation at the surface of Mars as observed by the Mars Science Laboratory Radiation Assessment Detector. *Journal of Geophysical Research: Planets*, 119, 1345–1358. <https://doi.org/10.1002/2013JE004525>
- Richardson, I. G. (2014). Identification of interplanetary coronal mass ejections at Ulysses using multiple solar wind signatures. *Solar Physics*, 289(10), 3843–3894. <https://doi.org/10.1007/s11207-014-0540-8>
- Richardson, I. G., & Cane, H. V. (1995). Regions of abnormally low proton temperature in the solar wind (1965–1991) and their association with ejecta. *Journal of Geophysical Research*, 100(A12), 23,397–23,412. <https://doi.org/10.1029/95JA02684>

- Richardson, I. G., & Cane, H. V. (2010). Near-Earth interplanetary coronal mass ejections during solar cycle 23 (1996–2009): Catalog and summary of properties. *Solar Physics*, 264, 189–237. <https://doi.org/10.1007/s11207-010-9568-6>
- Stone, E., Frandsen, A., Mewaldt, R., Christian, E., Margolies, D., Ormes, J., & Snow, F. (1998). The Advanced Composition Explorer. *Space Science Reviews*, 86(1), 1–22. <https://doi.org/10.1023/A:1005082526237>
- Temmer, M., Rollett, T., Möstl, C., Veronig, A. M., Vršnak, B., & Odstrčil, D. (2011). Influence of the ambient solar wind flow on the propagation behavior of interplanetary coronal mass ejections. *The Astrophysical Journal*, 743(2), 101.
- von Rosenvinge, T. T., Reames, D. V., Baker, R., Hawk, J., Nolan, J. T., Ryan, L., ... Wiedenbeck, M. E. (2008). The high energy telescope for STEREO. *Space Science Reviews*, 136(1), 391–435. <https://doi.org/10.1007/s11214-007-9300-5>
- Vršnak, B., Ruždjak, D., Sudar, D., & Gopalswamy, N. (2004). Kinematics of coronal mass ejections between 2 and 30 solar radii—What can be learned about forces governing the eruption? *Astronomy and Astrophysics*, 423(2), 717–728.
- Vršnak, B., Žic, T., Vrbanec, D., Temmer, M., Rollett, T., Möstl, C., ... Shanmugaraju, A. (2013). Propagation of interplanetary coronal mass ejections: The drag-based model. *Solar Physics*, 285(1), 295–315. <https://doi.org/10.1007/s11207-012-0035-4>
- Vršnak, B., Temmer, M., Žic, T., Taktakishvili, A., Dumbović, M., Möstl, C., ... Odstrčil, D. (2014). Heliospheric propagation of coronal mass ejections: Comparison of numerical WSA-ENLIL+Cone model and analytical drag-based model. *The Astrophysical Journal Supplement Series*, 213(2), 21.
- Vršnak, B., & Žic, T. (2007). Transit times of interplanetary coronal mass ejections and the solar wind speed. *Astronomy and Astrophysics*, 472(3), 937–943. <https://doi.org/10.1051/0004-6361:20077499>
- Wang, C., Du, D., & Richardson, J. D. (2005). Characteristics of the interplanetary coronal mass ejections in the heliosphere between 0.3 and 5.4 AU. *Journal of Geophysical Research*, 110, A10107. <https://doi.org/10.1029/2005JA011198>
- Wimmer-Schweingruber, R. F., Crooker, N. U., Balogh, A., Bothmer, V., Forsyth, R. J., Gazis, P., ... Zurbuchen, T. H. (2006). Understanding interplanetary coronal mass ejection signatures. *Space Science Reviews*, 123(1), 177–216. <https://doi.org/10.1007/s11214-006-9017-x>
- Wimmer-Schweingruber, R. F., Köhler, J., Hassler, D. M., Guo, J., Appel, J.-K., Zeitlin, C., ... Cucinotta, F. (2015). On determining the zenith angle dependence of the Martian radiation environment at Gale crater altitudes. *Geophysical Research Letters*, 42, 10,557–10,564. <https://doi.org/10.1002/2015GL066664>
- Winslow, R. M., Lugaz, N., Philpott, L. C., Schwadron, N. A., Farrugia, C. J., Anderson, B. J., & Smith, C. W. (2015). Interplanetary coronal mass ejections from MESSENGER orbital observations at Mercury. *Journal of Geophysical Research: Space Physics*, 120, 6101–6118. <https://doi.org/10.1002/2015JA021200>
- Winslow, R. M., Lugaz, N., Schwadron, N. A., Farrugia, C. J., Yu, W., Raines, J. M., ... Zurbuchen, T. H. (2016). Longitudinal conjunction between MESSENGER and STEREO A: Development of ICME complexity through stream interactions. *Journal of Geophysical Research: Space Physics*, 121, 6092–6106. <https://doi.org/10.1002/2015JA022307>
- Witasse, O., Sánchez-Cano, B., Mays, M. L., Kajdić, P., Opgenoorth, H., Elliott, H. A., ... Altobelli, N. (2017). Interplanetary coronal mass ejection observed at STEREO-A, Mars, comet 67P/Churyumov-Gerasimenko, Saturn, and New Horizons en route to Pluto: Comparison of its Forbush decreases at 1.4, 3.1, and 9.9 AU. *Journal of Geophysical Research: Space Physics*, 122, 7865–7890. <https://doi.org/10.1002/2017JA023884>
- Wood, B. E., Wu, C.-C., Lepping, R. P., Nieves-Chinchilla, T., Howard, R. A., Linton, M. G., & Socker, D. G. (2017). A STEREO survey of magnetic cloud coronal mass ejections observed at Earth in 2008–2012. *The Astrophysical Journal Supplement Series*, 229(2), 29.
- Yashiro, S., Gopalswamy, N., Michalek, G., St. Cyr, O. C., Plunkett, S. P., Rich, N. B., & Howard, R. A. (2004). A catalog of white light coronal mass ejections observed by the SOHO spacecraft. *Journal of Geophysical Research*, 109, A07105. <https://doi.org/10.1029/2003JA010282>
- Zhao, L.-L., & Zhang, H. (2016). Transient galactic cosmic-ray modulation during solar cycle 24: A comparative study of two prominent Forbush decrease events. *The Astrophysical Journal*, 827(1), 13.
- Žic, T., Vršnak, B., & Temmer, M. (2015). Heliospheric propagation of coronal mass ejections: Drag-based model fitting. *The Astrophysical Journal Supplement Series*, 218(2), 32.